Computers and Concrete, Vol. 1, No. 3 (2004) 227-248
DOI: http://dx.doi.org/10.12989/cac.2004.1.3.227

An experimental-computational investigation of fracture in brittle materials

K. De Proft†

Mechanics of Materials and Constructions, Vrije Universiteit Brussel, Pleinlaan 2, 1050 Brussels, Belgium

G. N. Wells‡, L. J. Sluys‡†

Department of Faculty of Civil Engineering and Geosciences, Delft University of Technology, Stevinweg 1, 2628 CN Delft, The Netherlands

W. P. De Wilde

Department of Mechanics of Materials and Constructions, Vrije Universiteit Brussel, Pleinlaan 2, 1050 Brussels, Belgium
(Received August 13, 2003, Accepted July 12, 2004)

Abstract. A combined experimental-computational study of a double edge-notched stone specimen subjected to tensile loading is presented. In the experimental part, the load-deformation response and the displacement field around the crack tip are recorded. An Electronic Speckle Pattern Interferometer (ESPI) is used to obtain the local displacement field. The experimental results are used to validate a numerical model for the description of fracture using finite elements. The numerical model uses displacement discontinuities to model cracks. At the discontinuity, a plasticity-based cohesive zone model is applied for monotonic loading and a combined damage-plasticity cohesive zone model is used for cyclic loading. Both local and global results from the numerical simulations are compared with experimental data. It is shown that local measurements add important information for the validation of the numerical model. Consequently, the numerical models are enhanced in order to correctly capture the experimentally observed behaviour.

Keywords: cohesive zone models; combined damage-plasticity.

1. Introduction

A variety of computational techniques exist to describe the fracture behaviour of quasi-brittle materials. These numerical models must be able to simulate the behaviour of quasi-brittle materials under different loading conditions. Therefore, experimental data is very important to verify models.

† Currently, Royal Military Academy, Civil Engineering Department, Renaissancelaan 30, 1000 Brussels, Belgium
‡ Assistant Professor
‡† Professor

Firstly, experimental data is needed to determine if the proposed numerical models are capable of simulating the observed behaviour. Secondly, experimental data is necessary to obtain model parameters. Conversely, numerical simulations can be used to improve experiments. The link between experimental and computational work is extremely important. In this paper, a combined experimental-computational study of a double-edge notched (DEN) stone specimen subjected to tensile loading is presented. In the first section, the experimental set-up is presented and experimental results are discussed. Monotonic as well as cyclic loadings are considered. Then, a discontinuous finite element formulation, in combination with a plasticity-based cohesive model and a combined damage-plasticity cohesive model, is introduced for the simulation of the DEN-tensile tests. Finally, the numerical results are compared with experimental data.

2. Experimental set-up

For the experiments, a natural limestone named *Massangis* is used. This type of limestone is frequently used for restoration purposes. The stone *Massangis* is available in several varieties and is mined in Massangis, France. The variety *Massangis Roche Jaune* is used for the experiments.

All specimens are 120 mm high and 50 mm wide. The thickness is 11 mm. Notches 7 mm deep and 1 mm wide are sawn in the middle of both sides of the specimen. The geometry of the specimen is shown in Fig. 1. Two Linear Variable Differential Transducers (LVDT) are used for the measurement of the deformation. The LVDT's are placed over the notches on each side of the specimen, as indicated in Fig. 1. The vertical measuring range of the LVDT's is 20 mm. Due to the notches, the crack will initiate within the range of the LVDT's. When a macro crack starts to grow, the deformations tend to localize, with other parts of the specimen unloading. When the crack is not within the range of the LVDT's, or when the measuring range of the LVDT's is too large, a snap-back will occur, making the measurement of the post-peak behaviour impossible. When the crack is situated within the range of the LVDT's, the measured deformation increases gradually. In this case,

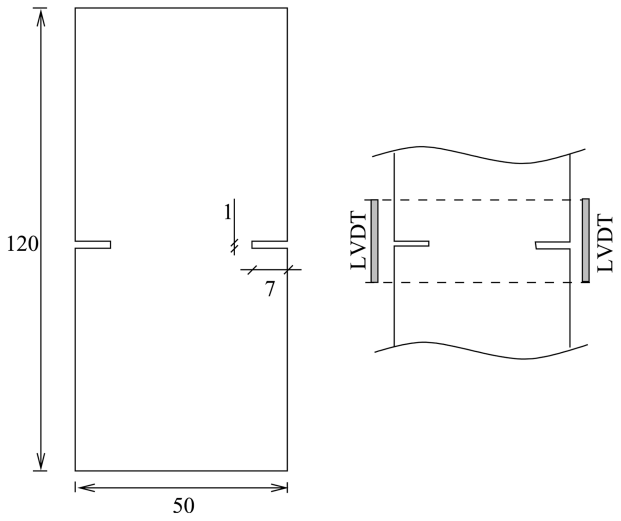

Fig. 1 Geometry of the specimen (all dimensions in mm) and placement of LVDT

the average signal of the LVDT's can be used as the control signal for the test. The average signal (CMOD – Crack Mouth Opening Displacement) is also used in the load-deformation response. The experiments are performed with an INSTRON 4505 testing bench. The specimens are glued directly to the loading platens, so that the boundaries of the specimen cannot rotate. Tensile loading is applied by means of a uniform vertical displacement of the boundary. For the cyclic loading cases, two unloading-reloading sequences are carried out in the post-peak regime. All tests were performed under displacement control at a rate of 0.3 μm/s. An Electronic Speckle Pattern Interferometer (ESPI) device was used to record the local displacement field at different load steps. The specimen was illuminated by laser light and speckles appear on the lighted surface. A CCD camera captures the reflected light. By subtracting different speckle patterns, interference fringes are formed. These fringes contain information about the displacement of the studied specimen. Unlike strain gauges, there is no contact with the specimen and the strain field (which can be computed with the supplied software) of a section of the specimen can be studied. A user-defined border restricts the measuring area of the ESPI. Within this border, a reference point is defined. The displacements of all material points situated inside the border are relative to the reference point. In order to make a comparison with numerical results, five paths are defined along which the displacements are monitored at several load steps. The different load paths and the position of the reference point are shown in Fig. 2. Subtracting the displacements in the y-direction along path 1 from the corresponding displacements along path 2 gives the deformation between those two paths.

3. Experimental results

3.1 Monotonic loading

A typical measured load-deformation response is shown in Fig. 3. The behaviour is nearly linear until the peak load. Just before peak load, the response deviates slightly from the linear path. This indicates that some micro-cracking is occurring before the peak load has been reached. After the peak load, a sharp drop is observed, indicating a brittle response. At this stage, deformation localizes in a single macro crack and the behaviour is highly non-linear. Apart from the load-

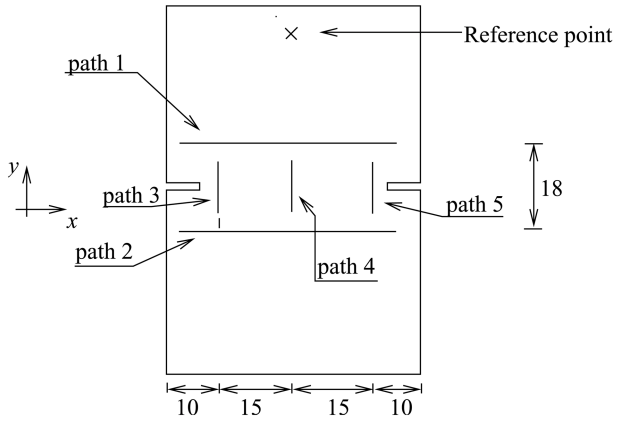

Fig. 2 Position of the reference point and paths for ESPI measurement

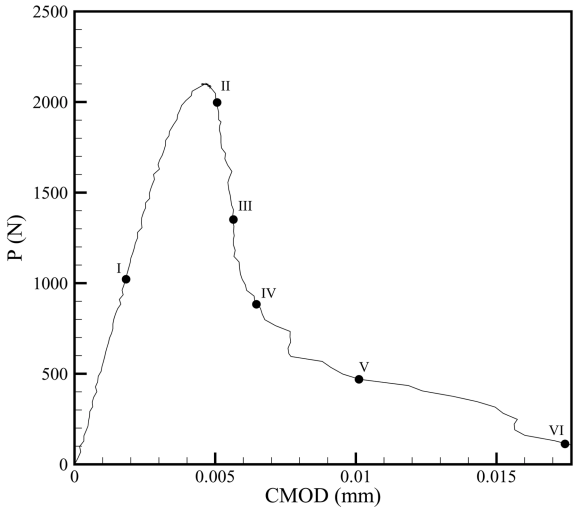

Fig. 3 Representative load-deformation response for monotonically loaded specimen

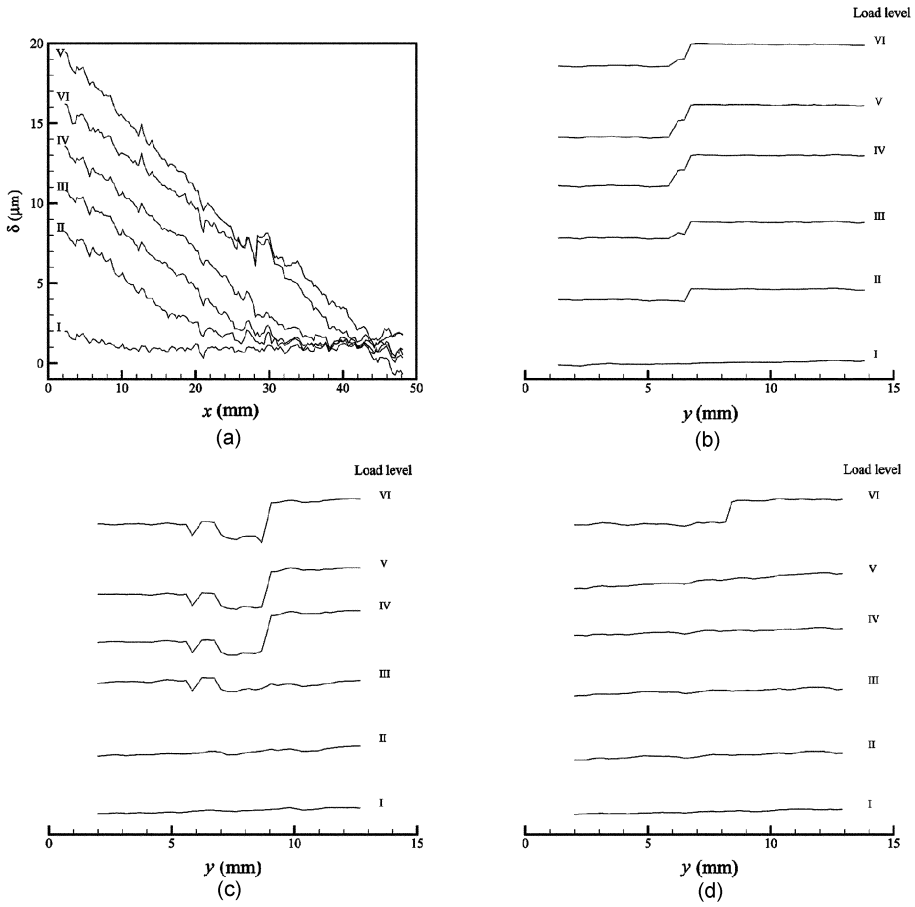

Fig. 4 (a) Deformations measured between path 1 and path 2, (b) displacements along path 3, (c) path 4 and (d) path 5 referred to the reference point

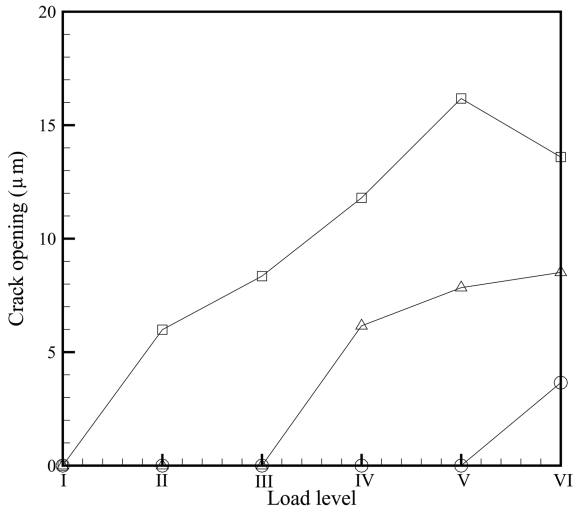

Fig. 5 Crack opening at right notch (circles), left notch (squares) and middle (triangles) for different load levels

deformation response, the displacement field in the vicinity of the crack tip is also recorded. Black dots in Fig. 3 indicate load levels at which snapshots of the displacement field within the defined border were taken. The deformations for various load levels, measured in the *y*-direction between path 1 and 2 are shown in Fig. 4(a). For load level I, the deformations are uniform. For all other load levels, the recorded deformations are highly non-uniform, indicating crack growth from the left to the right notch. The location of the crack tip during loading can be inferred from the deformations along each path. Near load level VI, the crack has crossed the complete specimen. Figs. 4(b)-4(d) show the displacements measured along path 3, 4 and 5. The values are relative to

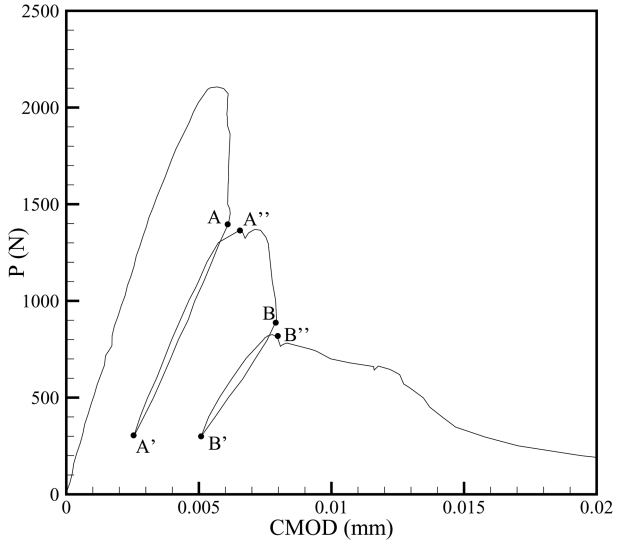

Fig. 6 Load-deformation response for cyclically loaded specimen

the reference point, hence no quantitative conclusions can be made, and no vertical axis is shown. Nevertheless, the results are very useful. As can be seen in Fig. 4, the crack which started at the left notch induced a jump in the displacements along path 3 (Fig. 4(b)). In the middle of the specimen (Fig. 4(c)) and at the right notch (Fig. 4(d)), the displacements are still continuous. At load level IV, the crack has reached the centre of the specimen, while the crack has crossed the entire specimen at load level VI. From the profiles in Fig. 4, the magnitude of the displacement jump can be computed. Again, by computing the relative difference, the influence of the reference point is eliminated. Fig. 5 shows the evolution of the crack opening on the left side (squares), the middle (triangles) and the right side (circles) of the specimen as a function of the load level.

The crack opening measured at the left notch first increases. At load level IV, a crack opening in the middle of the specimen is measured. Finally, at load level VI, the crack has reached the right notch. At this time, the crack opening at the left notch decreases again. This can also be observed in Fig. 4(a).

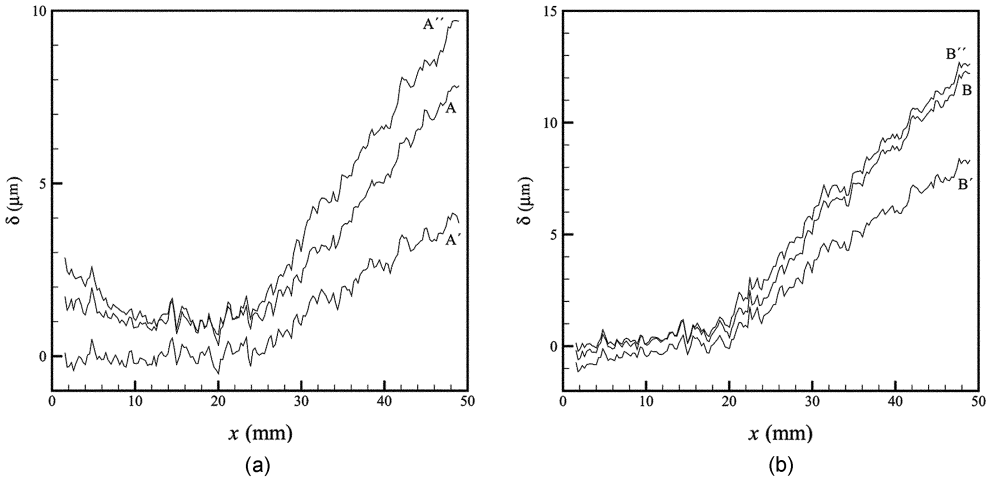

Fig. 7 Deformations before and after unloading and after reloading for (a) the first cycle and (b) the second cycle

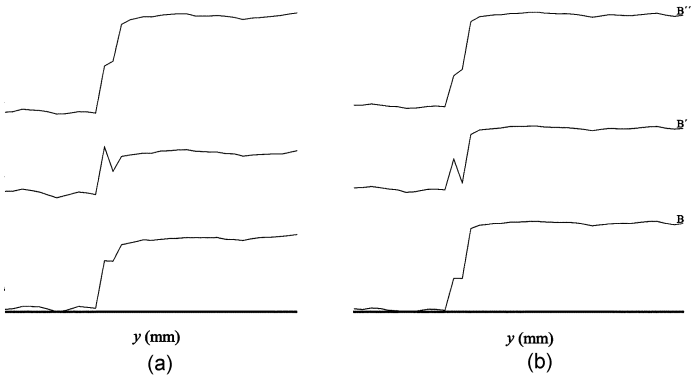

Fig. 8 Evolution of the displacements along path 5 for (a) the first cycle and (b) the second cycle

3.2. Cyclic loading

The DEN specimens were also subjected to cyclic loading. In all tests, two unloading cycles were introduced. A typical measured load-deformation response is shown in Fig. 6. Examining the load-deformation response, three issues should be emphasized:

- after complete unloading, crack closure is not complete;
- the unloading stiffness reduces with increasing deformation; and
- during the unloading/loading cycle, a small amount of energy is dissipated.

Black dots represent loads at which a snapshot of the displacement field was taken. The displacements along the predefined paths are extracted from the measurements. Only snapshots before and after unloading are shown. Again, the relative deformation between path 1 and path 2 is computed in order to remove the influence of the reference point. Fig. 7(a) shows the deformations before (A) and after (A') unloading and after reloading (A''). It is clear that, before unloading, a crack is growing from the right notch. As was the case for monotonic loading, the deformations are highly non-uniform. Then, the tensile loading is decreased until $P = 300$ N. When the deformations are studied after unloading (Fig. 7(a) - A'), it is clear that the specimen is divided into two regions:

- a first part where deformations are vanishing when the load is decreasing, indicating elastic or damage behaviour;
- a second part where, after unloading, permanent deformations occur.

After reloading (Fig. 7(a) - A'), the deformations return to approximately the same levels as before unloading (note that the difference between A and A'' in Fig. 7(a) is due to the difference in CMOD when the snapshot was taken). The loading-unloading-reloading cycle is repeated further in the post-peak branch. Examining Fig. 7(b), the same conclusions can be drawn. Note that the permanent deformations after unloading have increased, compared with the first cycle (compare A' in Fig. 7(a) with B' in Fig. 7(b)).

Displacements along path 5 (see Fig. 2) are shown in Fig. 8. The values are referred to the reference point and are only as an indication of the evolution of the displacement jumps. From Figs. 8(a) and 8(b), it is clear that after unloading the crack does not completely close.

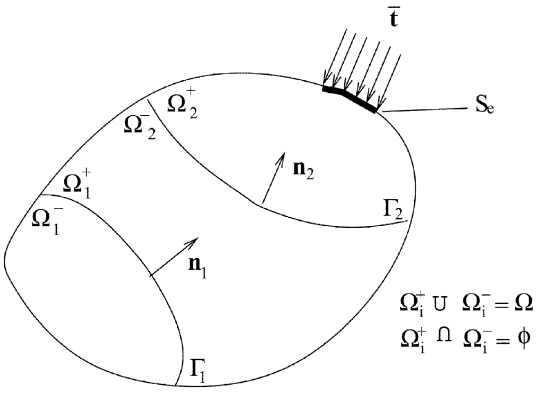

Fig. 9 Body Ω crossed by two discontinuities

4. Numerical model

4.1. Discontinuous finite elements based on partitions of unity

A cohesive zone model, with elastic continuum, is used to model the failure. A discontinuous finite element formulation which can represent arbitrary discontinuities is used for the description of fracture within finite elements. Discontinuous functions are added to the approximation basis, allowing discontinuities to propagate through the finite element mesh (Moës, *et al.* 1999, Wells and Sluys 2001). This is a very important advantage over interface elements, which allow discontinuities to propagate only along element boundaries.

Consider the body Ω in Fig. 9 which is crossed by discontinuities. A discontinuous displacement field can be decomposed as (for non-intersecting discontinuities):

$$\mathbf{u} = \hat{\mathbf{u}} + \sum_{i=1}^{m} H_{\Gamma_i} \tilde{\mathbf{u}}_i \tag{1}$$

where $\mathbf{u}$ is the displacement field, $\hat{\mathbf{u}}$ and $\tilde{\mathbf{u}}$ are continuous functions and H_{Γ_i} is the Heaviside function ($H_{\Gamma_i} = 1$ if $\mathbf{x} \in \Omega_i^+$, $H_{\Gamma_i} = 0$ otherwise), and m is the number of discontinuities. The infinitesimal strain field is obtained by taking the symmetric gradient of Eq. (1):

$$\boldsymbol{\varepsilon} = \nabla^s \hat{\mathbf{u}} + \sum_{i=1}^{m} H_{\Gamma_i} \nabla^s \tilde{\mathbf{u}}_i + \sum_{i=1}^{m} \delta_{\Gamma_i} (\tilde{\mathbf{u}}_i \otimes \mathbf{n}_i)^s \tag{2}$$

where $\mathbf{n}_i$ is the normal to discontinuity surface i and δ_{Γ_i} is the Delta function corresponding to discontinuity surface i. In terms of a finite element basis, the displacement field can be interpolated as:

$$\mathbf{u} = \mathbf{N}\mathbf{a} + \sum_{i=1}^{m} H_{\Gamma_i} \mathbf{N}\mathbf{b}_i \tag{3}$$

where $\mathbf{N}$ is the matrix containing the finite element shape functions, $\mathbf{a}$ are the 'regular' degrees of freedom and $\mathbf{b}_i$ are the 'enhanced' degrees of freedom related to crack i. For each crack, an additional set of degrees of freedom are added. The resulting linearized governing equations can be expressed as:

$$\begin{bmatrix} \mathbf{K}_{aa} & \mathbf{K}_{ab_1} & \cdots & \mathbf{K}_{ab_m} \\ \mathbf{K}_{b_1a} & \mathbf{K}_{b_1b_1} & \cdots & \mathbf{K}_{b_1b_m} \\ \vdots & \vdots & \vdots & \vdots \\ \mathbf{K}_{b_ma} & \mathbf{K}_{b_mb_1} & \cdots & \mathbf{K}_{b_mb_m} \end{bmatrix} \begin{Bmatrix} d\mathbf{a} \\ d\mathbf{b}_1 \\ \vdots \\ d\mathbf{b}_m \end{Bmatrix} = \begin{Bmatrix} \mathbf{f}_a^{ext,\,t+\Delta t} \\ \mathbf{0} \\ \mathbf{0} \\ \mathbf{0} \end{Bmatrix} - \begin{Bmatrix} \mathbf{f}_a^{int,\,t} \\ \mathbf{f}_{b_1}^{int,\,t} \\ \vdots \\ \mathbf{f}_{b_m}^{int,\,t} \end{Bmatrix} \tag{4}$$

where

$$\mathbf{K}_{aa} = \int_{\Omega} \mathbf{B}^T \mathbf{C}^e \mathbf{B} \, d\Omega \tag{5a}$$

$$\mathbf{K}_{ab_j} = \int_\Omega H_{\Gamma_j} \mathbf{B}^T \mathbf{C}^e \mathbf{B} d\Omega \tag{5b}$$

$$\mathbf{K}_{b_j a} = \int_\Omega H_{\Gamma_j} \mathbf{B}^T \mathbf{C}^e \mathbf{B} d\Omega \tag{5c}$$

$$\mathbf{K}_{b_i b_j} = \int_\Omega H_{\Gamma_i} H_{\Gamma_j} \mathbf{B}^T \mathbf{C}^e \mathbf{B} d\Omega \tag{5d}$$

$$\mathbf{K}_{b_j b_j} = \int_\Omega \mathbf{B}^T \mathbf{C}^e \mathbf{B} d\Omega + \int_{\Gamma_j} \mathbf{N}^T \mathbf{D} \mathbf{N} d\Gamma \tag{5e}$$

where $\mathbf{C}^e$ is the elastic continuum material tensor (in matrix form) and $\mathbf{D}$ is the material tangent for the cohesive law on the discontinuity. Note that all stiffness contributions in Eq. (5) are very similar. The crucial difference between the terms in Eq. (5) is the presence of the Heaviside function. This makes the finite element implementation relatively simple. It is assumed that the considered element is crossed by discontinuity *j* and influenced by discontinuity *i*. During a simulation, discontinuities can be extended by activating 'enhanced' degrees of freedom. Detailed information on the discontinuity model can be found in Wells (2001) and De Proft (2003).

4.1.1. Implementation aspects

For the propagation of a discontinuity, a criterion is evaluated in the elements in front of the crack tips. For mode-I cracking, a discontinuity can be initiated perpendicular to the maximal principal stress direction when the tensile strength in the element is exceeded. More generally, a yield surface can be used to determine whether a discontinuity should propagate. In this case, a bifurcation analysis may be necessary to compute the propagation direction. Discontinuities are allowed to develop at the end of a time step. As was stated by Wells (2001) this procedure ensures quadratic convergence of the Newton-Raphson solution process. Once a discontinuity has been extended, the nodes of the crossed element are enhanced. The nodes on the element edge touched by a discontinuity are restrained, so that the displacement jump at the tip is zero. During a computation, only one discontinuity is allowed to cross an element. When a discontinuity enters an element which is already crossed by a discontinuity, the discontinuity is stopped. When two discontinuities reach the same elastic element, the discontinuities can join. In order to ensure adequate integration of crossed elements, the integration scheme is changed in these elements (Moës, *et al.* 1999, Wells and Sluys 2001).

4.2. A plasticity based cohesive zone model

The behaviour at a discontinuity is described by a plasticity-based cohesive zone model. The adopted plasticity model was proposed by Carol, *et al.* (1997) for use in interface elements. Consequently, the plastic yield function is given in the traction space. A hyperbolic yield surface is introduced according to:

$$f = T_t^2 - (c - T_n \tan\phi)^2 + (c - f_t \tan\phi)^2 \tag{6}$$

where $\mathbf{T} = (T_n, T_t)$ are the normal and tangential component of the traction vector, c is the cohesion, f_t the tensile strength and ϕ the internal friction angle of the material. For tension, an associative flow rule is adopted. The evolution of the yield surface is governed by the decrease in tensile strength and cohesion throughout the computation according to:

$$f_t = f_{t0}\left(1 - \frac{W_{cr}}{G_f^I}\right) \tag{7a}$$

$$c = c_0\left(1 - \frac{W_{cr}}{G_f^{II}}\right) \tag{7b}$$

where f_{t0} and c_0 are the initial values for the tensile strength and the cohesion, G_f^I is the mode-I fracture energy, G_f^{II} is the mode-II fracture energy and W_{cr} is the energy dissipated in the development of a unit area of traction free crack. The energy dissipated incrementally is defined as:

$$dW_{cr} = T_n d\Delta_n^{pl} + T_t d\Delta_t^{pl} \tag{8}$$

where $\boldsymbol{\Delta} = \{\Delta_n^{pl}, \Delta_t^{pl}\}$ are the normal and tangential components of the plastic separation vector. Eq. (7) ensures that the total mode-I fracture energy/mode-II fracture energy is dissipated when the tensile strength/cohesion vanishes. Furthermore, the decrease in tensile strength and cohesion is coupled; when a material is damaged due to tensile loading, both the tensile strength and the cohesion decrease.

The tangential stiffness and the stress update are obtained with classical elasto-plastic equations. The tractions are defined through:

$$\mathbf{T} = \mathbf{D}^e(\boldsymbol{\Delta} - \boldsymbol{\Delta}^{pl}) \tag{9}$$

where $\mathbf{D}^e$ is the elastic stiffness of the discontinuity. The plastic deformation rate is defined as:

$$\dot{\boldsymbol{\Delta}}^{pl} = \dot{\lambda}\mathbf{m} \tag{10}$$

where $\dot{\lambda}$ is the plastic multiplier rate and $\mathbf{m} = \partial f/\partial \mathbf{T}$ is the direction of plastic flow. The plastic deformation rate can be introduced in Eq. (9), leading to:

$$\dot{\mathbf{T}} = \mathbf{D}^e(\dot{\boldsymbol{\Delta}} - \dot{\lambda}m) \tag{11}$$

The plastic multiplier rate can be obtained through the consistency equation:

$$\dot{\lambda} = \frac{\mathbf{m}^T\mathbf{D}^e\dot{\boldsymbol{\Delta}}}{\mathbf{m}^T\mathbf{D}^e\mathbf{m} - h} \tag{12}$$

where h is the hardening/softening modulus. Inserting the result for the plastic multiplier into Eq. (11) yields the tangential stiffness:

$$\dot{\mathbf{T}} = \left[\mathbf{D}^e - \frac{\mathbf{D}^e\mathbf{m}\mathbf{m}^T\mathbf{D}^e}{\mathbf{m}^T\mathbf{D}^e\mathbf{m} - h}\right]\dot{\boldsymbol{\Delta}} = \mathbf{D}\dot{\boldsymbol{\Delta}} \tag{13}$$

The tangential stiffness can be inserted into the finite element equations (see Eq. (5)). The elastic penalty stiffness is chosen to be very high, in theory infinite, in order to suppress spurious elastic deformations at the discontinuity. Since a discontinuity is only inserted when the yield surface is violated, the jump is completely inelastic. It can be shown that when including a high elastic stiffness, Eq. (13) is reduced to the strong discontinuity equation, (De Proft 2003, Simo, *et al.* 1993, Oliver, *et al.* 2003, Oliver 2000):

$$(\dot{\mathbf{u}} \otimes \mathbf{n})^s = \dot{\bar{\lambda}} \frac{\partial f}{\partial \boldsymbol{\sigma}} \tag{14}$$

where $\dot{\bar{\lambda}}$ bounded plastic multiplier rate and f is the yield function. Eq. (14) implies that the jump in the discontinuity is completely plastic.

4.3. A combined damage-plasticity cohesive zone model

In order to model the decrease in unloading stiffness and the accumulation of permanent deformations for the case of cyclic loading, a combined damage-plasticity model is used. A continuum model is degenerated to a constitutive relationship on a surface. The combined model uses the effective stress concept and the principle of strain equivalence. During loading, microcracks develop in the material. Due to these microcracks, the stresses are redistributed over the undamaged material bonds. Plastic deformations can only occur in the intact material. The stress in the intact material, the effective stress, is connected to the homogenized stress by a damage variable d,

$$\hat{\boldsymbol{\sigma}} = \frac{\boldsymbol{\sigma}}{(1-d)} \tag{15}$$

where $\hat{\boldsymbol{\sigma}}$ is the effective stress tensor, and $\boldsymbol{\sigma}$ is the homogenized stress tensor. As plastic deformations develop in an undamaged material skeleton, the constitutive relation can be written in terms of effective stresses,

$$\hat{\boldsymbol{\sigma}} = \mathbf{C}^e \boldsymbol{\varepsilon}^e = \mathbf{C}^e (\boldsymbol{\varepsilon} - \boldsymbol{\varepsilon}^p) \tag{16}$$

where $\boldsymbol{\varepsilon}^e$ is the elastic strain tensor. The yield function is formulated in the effective stress space

$$f^p = \hat{\phi}(\hat{\boldsymbol{\sigma}}) - \bar{\sigma}(\kappa^p) \tag{17}$$

where $\hat{\phi}$ is a scalar-valued function, $\bar{\sigma}$ is the yield strength of the material and κ^p is a strainlike internal variable.

Assume the following one dimensional yield surface:

$$f^p = \sigma - (f_{t0} + h\kappa^p) \tag{18}$$

where σ is the homogenized stress in the material, h is the hardening modulus, f_{t0} is the initial tensile strength. The yield surface given in Eq. (18) must be rewritten in the effective stress space. If damage and plasticity are assumed to start simultaneously, the damage variable is equal to zero when the yield surface is first reached (when $\kappa^p = 0$). The projection of the initial value for the tensile strength into the effective stress space is given by

$$\hat{f}_{t0} = \frac{f_{t0}}{(1-d)} = f_{t0} \tag{19}$$

and the yield function (18) can be expressed in effective stresses:

$$f^p = \hat{\sigma} - (f_{t0} + h\kappa^p) \tag{20}$$

The plasticity model must be completed with a damage model. The damage in a material must grow when the damage loading function is violated:

$$f^d = \varepsilon^{eq} - \kappa^d > 0 \tag{21}$$

where ε^{eq} is a scalar 'equivalent strain' and κ^d is a history parameter. The equivalent strain is an invariant of the strain tensor. The model will later be degenerated to a cohesive surface relationship, and it is physically intuitive to make the damage-driving scalar a function of the displacement jump. The internal variable represents the largest value of the equivalent strain reached. When damage grows (Eq. (21)), the damage variable is updated via

$$d = 1 - \frac{\kappa_i}{\kappa^d} exp[-\beta(\kappa^d - \kappa_i)] = 1 - \frac{q(\kappa^d)}{\kappa^d} \qquad \kappa^d > \kappa_i \tag{22}$$

where κ_i is the threshold of damage initiation, β is a model parameter and $q(\kappa^d)$ is a function defined as :

$$q(\kappa^d) = \kappa_i exp[-\beta(\kappa^d - \kappa_i)] \quad \kappa^d > \kappa_i \tag{23}$$

Combining Eqs. (15) and (16) and assuming an additive strain decomposition, the constitutive relation is written as

$$\boldsymbol{\sigma} = (1-d)\mathbf{C}^e(\boldsymbol{\varepsilon} - \boldsymbol{\varepsilon}^p) \tag{24}$$

The proposed continuum damage-plasticity model should be consistent with an incorporated discontinuity. The kinematical description for the strain field (2) is inserted into Eq. (24), yielding

$$\boldsymbol{\sigma} = (1-d)\mathbf{C}^e\left(\nabla^s\hat{\mathbf{u}} + \sum_{i=1}^{m} H_{\Gamma_i}\nabla^s\tilde{\mathbf{u}}_i + \sum_{i=1}^{m}\delta_{\Gamma_i}(\tilde{\mathbf{u}}_i \otimes \mathbf{n}_i)^s - \boldsymbol{\varepsilon}^p\right) \tag{25}$$

The stress field must remain bounded everywhere, which means that the delta function must cancel. For classical continuum plasticity models, the delta function is cancelled by making the plastic multiplier unbounded (Simo, *et al.* 1993). Following this line of reasoning, it can be assumed that the plastic strain field can be written in the same manner as the total strain field and that the continuum plastic strain is zero (since the continuum is assumed to remain elastic):

$$\boldsymbol{\sigma} = (1-d)\mathbf{C}^e\left(\nabla^s\hat{\mathbf{u}} + \sum_{i=1}^{m} H_{\Gamma_i}\nabla^s\tilde{\mathbf{u}}_i + \sum_{i=1}^{m}\delta_{\Gamma_i}(\tilde{\mathbf{u}}_i \otimes \mathbf{n}_i)^s - \sum_{i=1}^{m}\delta_{\Gamma_i}(\tilde{\mathbf{u}}_i^p \otimes \mathbf{n}_i)^s\right) \tag{26}$$

For a damage model, Oliver (2000) proposed to eliminate the Dirac-delta distribution by making the internal damage variable unbounded. In this case, the internal damage variable κ^d can be written in the following form:

$$\kappa^d = \breve{\kappa}^d + \delta_{\Gamma_i} \bar{\kappa}^d \tag{27}$$

where $\breve{\kappa}^d$ and $\bar{\kappa}^d$ are bounded. As was the case with the plastic multiplier, $\breve{\kappa}^d$ is set to zero assuming an elastic response in the continuum. Combining Eq. (22), Eq. (26) and Eq. (27), the delta function is eliminated and the stress at discontinuity i becomes:

$$\boldsymbol{\sigma} = \frac{q(\bar{\kappa}^d)}{\bar{\kappa}^d} \mathbf{C}^e [(\tilde{\mathbf{u}}_i \otimes \mathbf{n}_i)^s - (\tilde{\mathbf{u}}_i^p \otimes \mathbf{n}_i)^s] \qquad \text{for } \bar{\kappa}^d > 0 \tag{28}$$

The tractions can be computed from the stress field at the discontinuity, Eq. (28), according to

$$\mathbf{T}_i = \frac{q(\kappa^d)}{\bar{\kappa}^d} \mathbf{n}_i \mathbf{C}^e \mathbf{n}_i [\tilde{\mathbf{u}}_i - \tilde{\mathbf{u}}_i^p] \qquad \text{for } \bar{\kappa}^d > 0 \tag{29}$$

or,

$$\mathbf{T}_i = (1 - \omega) \mathbf{Q}_i^e [\tilde{\mathbf{u}}_i - \tilde{\mathbf{u}}_i^p] \quad \text{for } \bar{\kappa}^d > 0 \tag{30}$$

where ω is the discrete damage variable and $\mathbf{Q}_i^e = \mathbf{n}_i \mathbf{C}^e \mathbf{n}_i$ is the elastic acoustic tensor. Eq. (30) is very similar to the constitutive equation used in continuum problems (Simo and Ju 1987). The degenerated damage variable ω is analogous to the continuum damage variable, and the elastic material tensor is replaced by the elastic acoustic tensor. A major difference with continuum models is that the separation of the discontinuity is completely inelastic. The separation is decomposed into a damage (recoverable) part and into a plastic (irrecoverable) part. The plasticity model is solved in the effective traction space. The adopted yield surface is

$$f^p = \hat{T}_n - h\kappa^p \tag{31}$$

where $\hat{T}_n$ is the effective normal traction, h is the hardening/softening modulus and κ^p is the internal plastic variable. The evolution of damage is coupled to the damage loading function. This function is written in terms of an equivalent strain. However, strains are not defined in the discontinuity, so a new equivalent strain measure must be found. Based on intuitive reasoning, the positive normal separation opening is used, resulting in

$$f^d = \Delta_n - \bar{\kappa}^d \tag{32}$$

where Δ_n is the normal separation of the discontinuity and $\bar{\kappa}^d$ is the degenerated internal damage variable. Hence, damage is drive by normal opening only. When the damage loading function is violated, the degenerated damage variable is updated via

$$\omega = 1 - \frac{\kappa_i}{\bar{\kappa}^d} exp[-\beta(\bar{\kappa}^d)] \qquad \kappa^d > \kappa_i \tag{33}$$

where κ_i is the damage threshold and β is a model parameter.

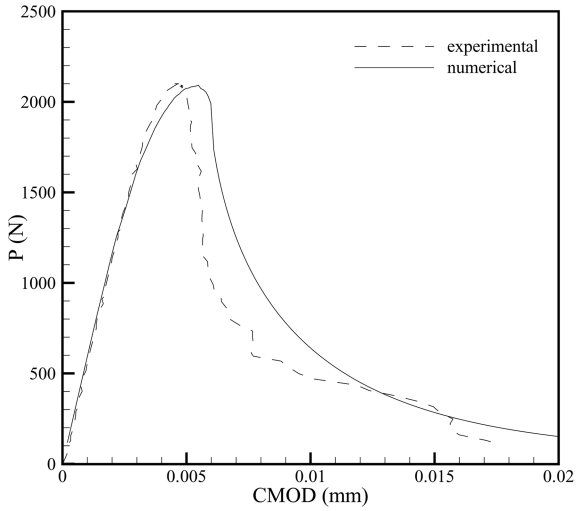

Fig. 10 Experimental and numerical load-deformation responses

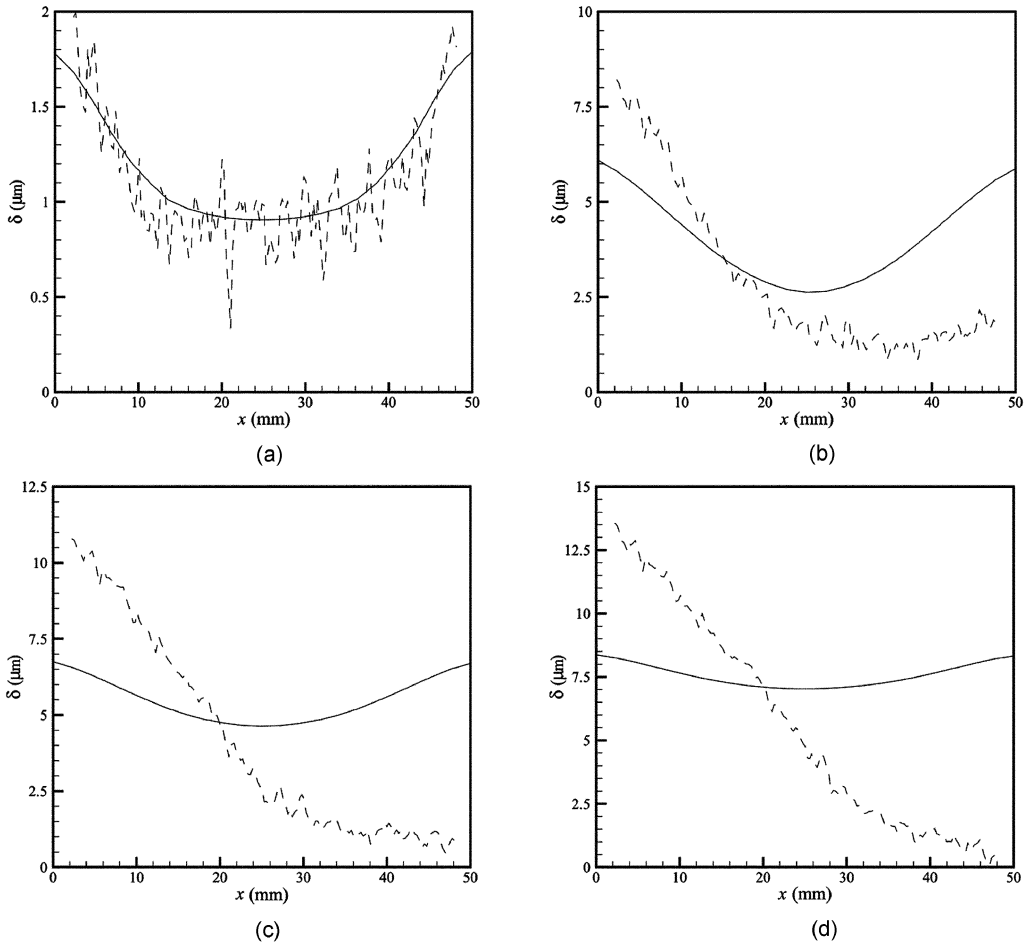

Fig. 11 Deformation profiles at (a) load level I, (b) load level II, (c) load level III and (d) load level IV (solid lines represent numerical results)

5. Numerical simulations vs experimental results

In this section, numerical simulations are performed with the discontinuous finite element model. Six-noded triangular elements are used. The mesh independency of this solution has already been discussed in Wells and Sluys (2001) and De Proft (2003). Focus here is placed on the careful comparison of experimental en computational results.

5.1. Monotonic loading

Simulations of the monotonic loading cases are performed with the plasticity-based cohesive zone model presented in section 4.2. For the first simulation, the following model parameters are adopted: $f_{t0} = 6.2$ MPa, $c_0 = 20$MPa, $\phi = 26.35$, $G_f^I = 0.04$N/mm and $G_f^{II} = 0.1$N/mm. The computed load-deformation response is shown in Fig. 10. As can be seen, a good fit between numerical simulations and experimental results is obtained. The computational response deviates slightly before the peak load from the experimental response. The peak load is captured well, while the experimental post-peak behaviour is more brittle. Apart from the global response, the growth of the crack and the displacements in the fracture zone have been considered. Fig. 11 compares the experimental deformation profiles at different load levels with the numerically computed values. Fig. 11(a) shows the deformation profile in the elastic stage. The numerical simulation is symmetric and in good agreement with measured deformations. Fig. 11(b) is a snapshot just after peak load. Clearly, the experimental deformation profile shows asymmetric crack growth, while for the numerical simulation the profile remains symmetric. In Figs. 11(c) and 11(d), the asymmetry in the experimental result increases, while the numerical simulations predict symmetric deformations. The model is not able to capture the experimental observations. The symmetric crack growth is a logical solution since the boundary value problem is symmetric about the centreline of the specimen. The numerical model needs to be modified in order to capture the experimentally observed deformations. Non-symmetric crack growth can be numerically triggered by:

- introducing an imperfection at a notch; or
- introducing bending, resulting in a non-uniform stress state.

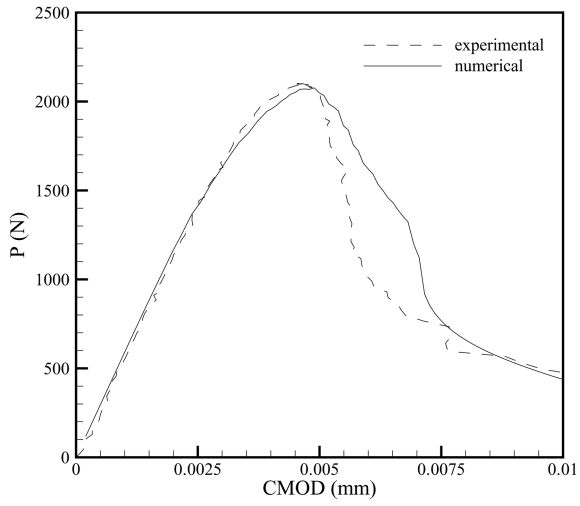

Fig. 12 Load-deformation response for non-symmetric crack growth due to a weaker element

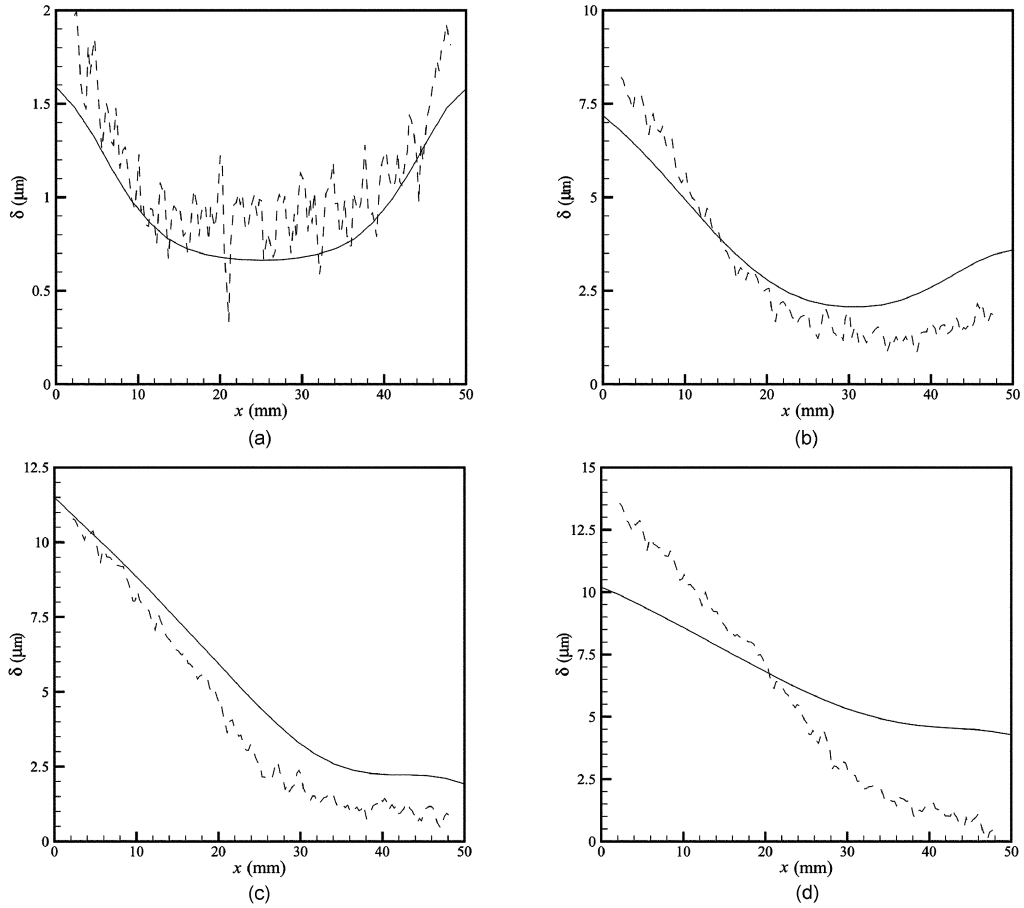

Fig. 13 Deformation profiles obtained for a weaker element for (a) load level I, (b) load level II, (c) load level III and (d) load level IV (solid lines represent numerical results)

Firstly, an element at the left notch is made slightly weaker. The tensile strength is decreased by 5%. Consequently, the crack starts earlier in this element and crack propagation may be non-symmetric. The model parameters are: $f_{t0} = 6.7$ MPa, $c_0 = 20$MPa, $\phi = 26.35$, G_f^I = 0.03N/mm and G_f^{II} = 0.1N/mm. The computed load-deformation response is shown in Fig. 12. Examining Fig. 12, two remarks can be made:

- the peak load is captured correctly; and
- just after the peak load, the computed post peak behaviour is more ductile. Around load level P = 1350 N, a drop in the load-deformation curve is observed. After the drop, the computed post peak behaviour is close to the experimentally measured response.

When the deformation profiles in Fig. 13 are studied, the sudden drop in the load deformation response may be explained. In the beginning, the computed deformation profiles follow the experimentally obtained curves. For the last load level, Fig. 13(d), the computed deformation profile

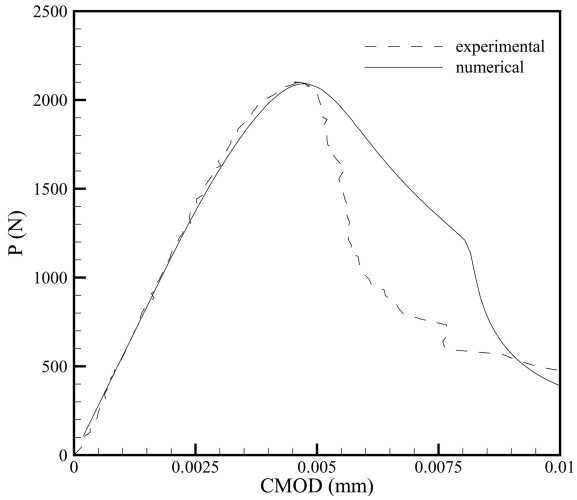

Fig. 14 Load-deformation response for DEN test with bending

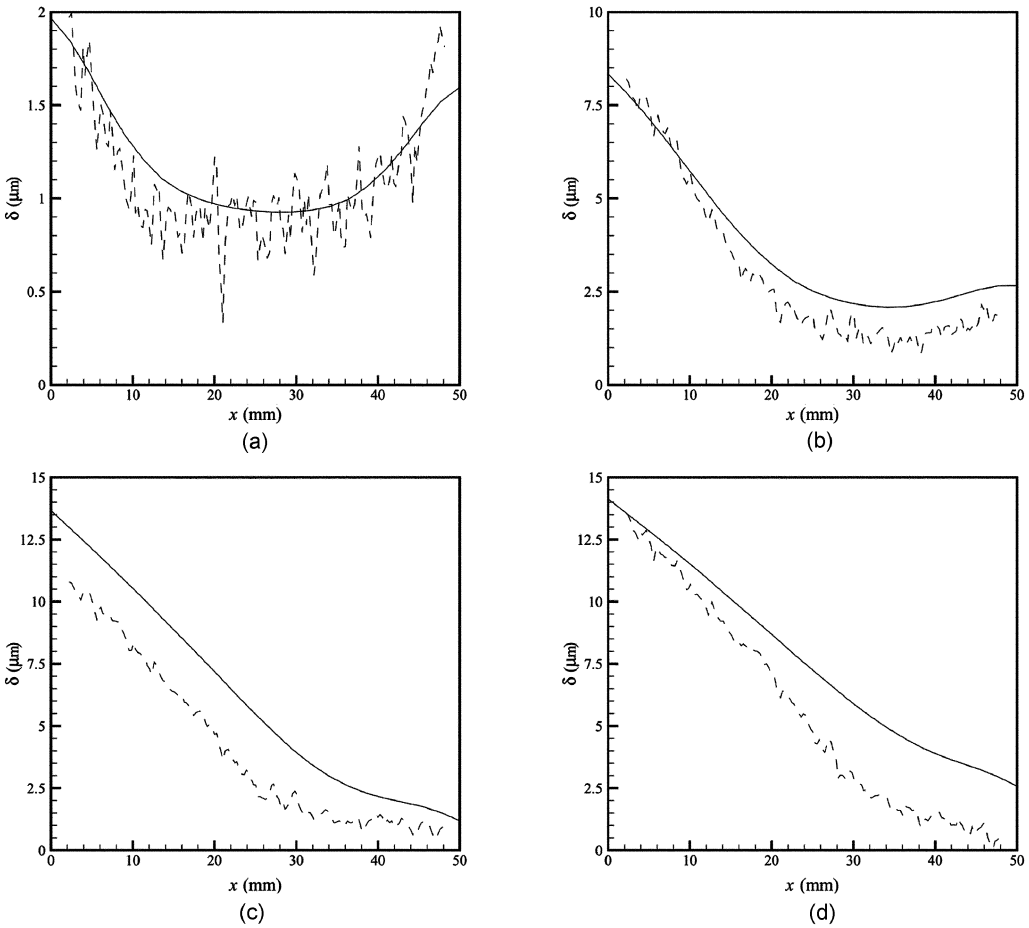

Fig. 15 Deformation profiles obtained for eccentric loading for (a) load level I, (b) load level II, (c) load level III and (d) load level IV (solid lines represent numerical results)

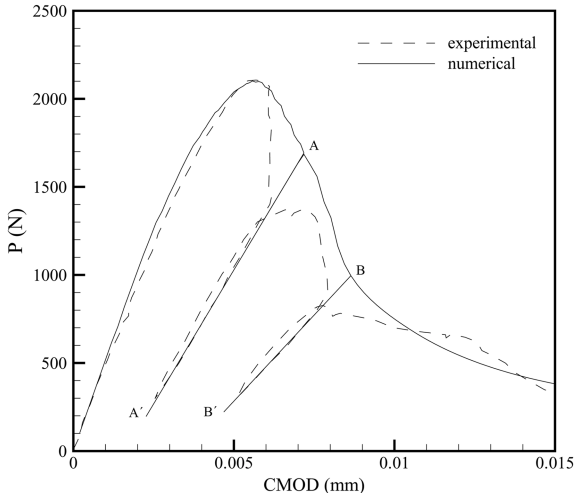

Fig. 16 Comparison of experimental and numerical (with material weakness) obtained load-deformation response for cyclic loading

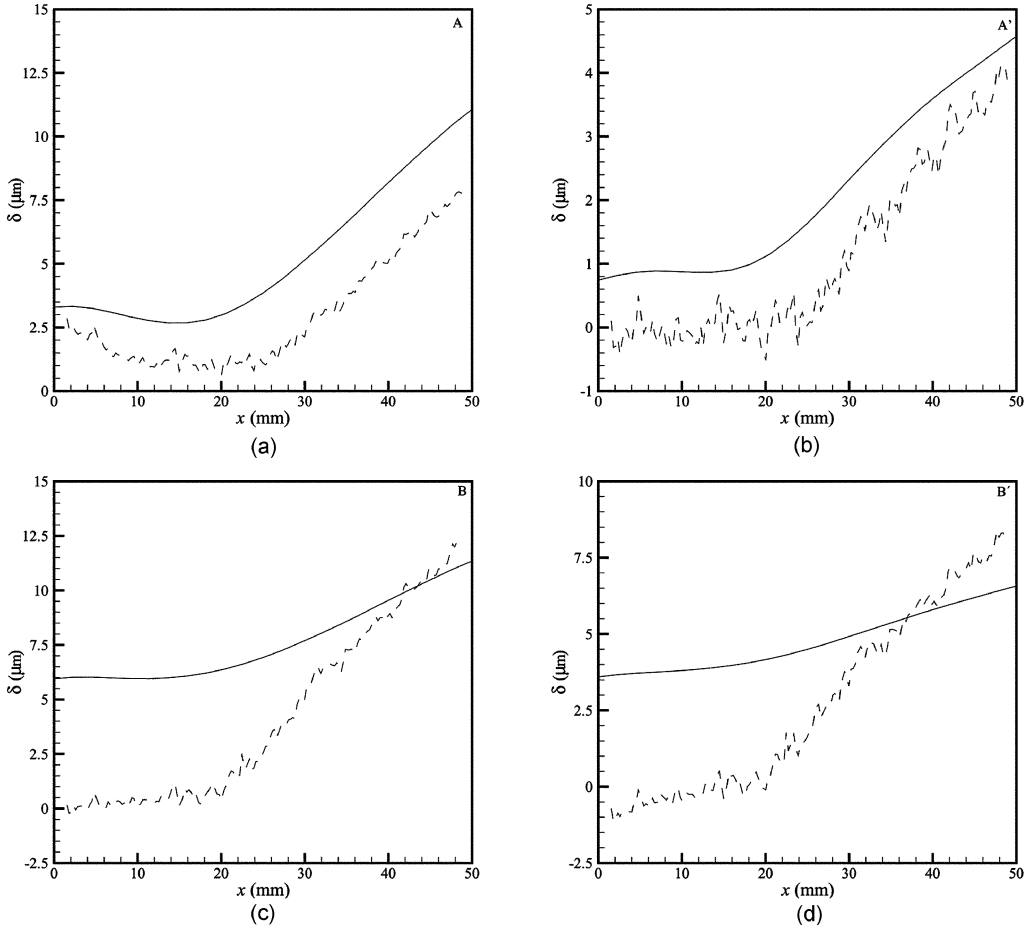

Fig. 17 Deformation profiles for (a) begin and (b) end unloading branch 1 and (c) begin and (d) end unloading branch 2 (solid lines represent numerical results)

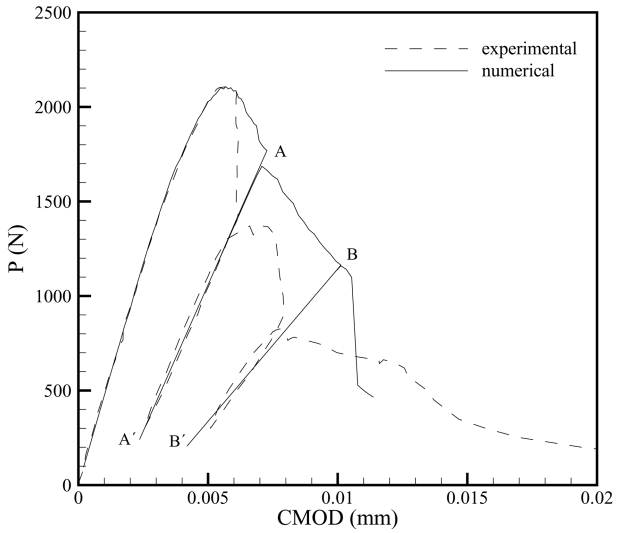

Fig. 18 Comparison of experimental and numerical (with added bending) obtained load-deformation response for cyclic loading

returns to a more uniform distribution. This is connected to the drop in the load-deformation curve. The drop is explained by the transition from a non-symmetric mode into a more uniform deformation mode.

The second way to incorporate non-symmetric crack propagation, eccentric loading, is is now examined. An eccentricity of $e = 2.2$ mm is adopted and the following model parameters are used: $f_{t0} = 7.3$ MPa, $c_0 = 20$MPa, $\phi = 26.35$, $G_f^I = 0.035$N/mm and $G_f^{II} = 0.1$N/mm .

The load-deformation response is shown in Fig. 14, and again the peak load is reproduced well. Furthermore, the drop in the load-deformation curve, already observed in Fig. 12, is also present and is more pronounced. The numerically obtained deformation profiles are compared with experimental results in Figs. 15(a)-15(d). For all load levels, the computed profiles are close to the experimental curves. Even after the drop in the load-deformation response, the computational results follow the experimental results remarkably well.

5.2. Cyclic loading

The cyclically loaded specimen is also simulated. The numerical modelling is performed with the combined damage-plasticity model, defined in section 4.3.

In a first simulation, non-symmetric crack growth is triggered by a weakened element at the right notch. The adopted model parameters are: $f_{t0} = 6.5$ MPa, $h = 27000$ N/mm^3 and $\beta = 400$. The experimentally and numerically obtained load-displacement responses are plotted in Fig. 16. Obviously, the proposed combined damage-plasticity model can capture the decrease of stiffness and the appearance of permanent deformations. The post peak behaviour of the numerical simulation is more ductile. The steep descent in the beginning of the post peak was not captured.

The computed deformation profiles are compared with experimental measured curves in Figs. 17(a)-17(d). Snapshots are taken at the beginning and the end of the unloading branches. For unloading branch 1, the deformation profiles are similar. After unloading (see Fig. 17(b)) the

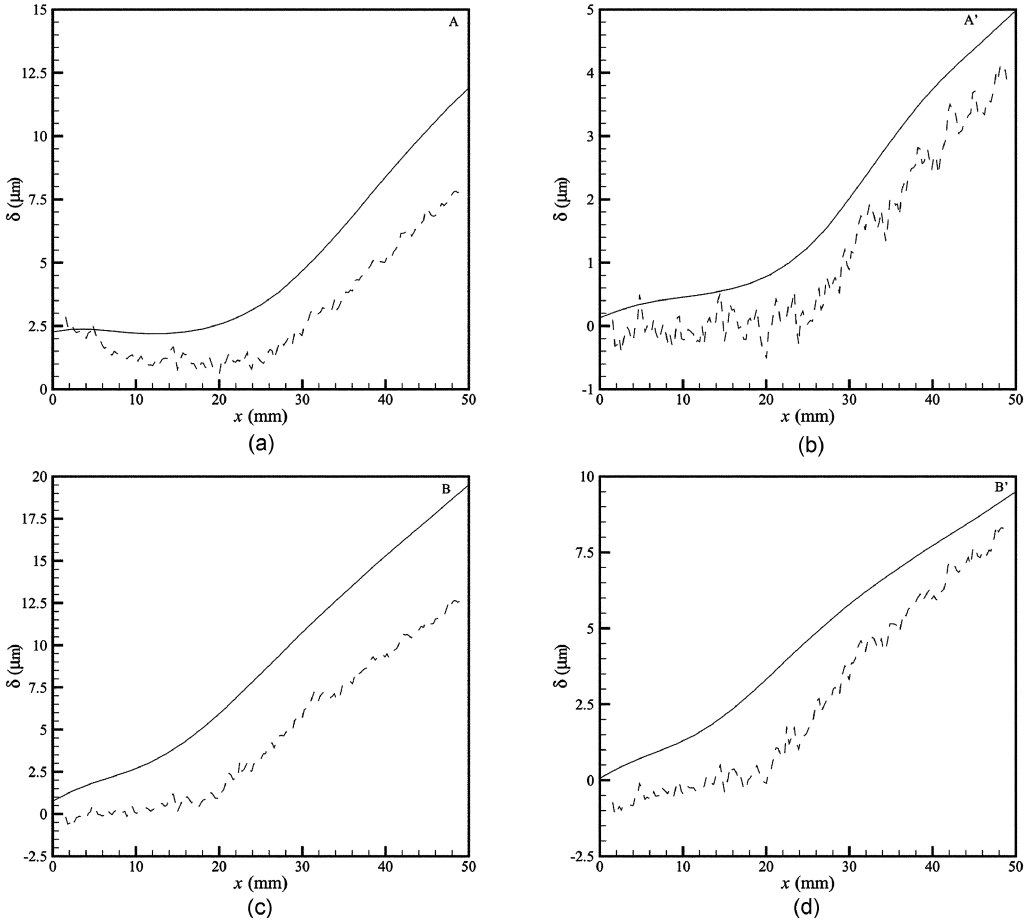

Fig. 19 Deformation profiles for (a) begin and (b) end unloading branch 1 and (c) begin and (d) end unloading branch 2 (solid lines represent numerical results)

calculation shows permanent deformations at the left side of the specimen while the experimental deformations largely disappear. This means that during the calculation, a discontinuity is already introduced at the left side, while in reality, the behaviour is still elastic. For the second unloading branch the difference is even more pronounced. The same simulations are repeated for non-symmetric crack growth triggered by an additional bending moment. The adopted model parameters are: $f_{t0} = 7.8$ MPa, $h = 27000$ N/mm^3 and $\beta = 400$. The obtained load-deformation curve is compared with the experimental result in Fig. 18. Again, the computed peak load is comparable with the experimental measured value, while the computed post peak behaviour is more ductile. The experimental and computed deformation profiles are compared in Figs. 19(a)-19(d). Compared with Fig. 17, the deformation profiles after unloading (Fig. 17(b)-Fig. 18(b)) are better captured when a bending moment is introduced. Furthermore, the computed deformations are higher than the measured ones.

6. Conclusions

In this paper, a combined experimental-computational study of the tensile behaviour of limestone has been presented. Both monotonic as well as cyclic loading was performed, with global and local measurements recorded. Globally, the load-deformation response was captured and locally, the displacement field around the crack tip was measured. It was shown that with the use of the ESPI technique, important information can be recorded. Moreover, the ESPI technique is very useful since there is no contact with the specimen, and consequently, the measurement does not interfere with the experimental process. Measurements showed that a displacement jump is present across the crack, motivating the use of a cohesive zone model. Measurements also showed that the obtained deformations are non-symmetric, and after unloading, permanent deformations were present.

For the numerical simulations, discontinuous finite elements were used in combination with a plasticity-based and a combined damage-plasticity cohesive zone model. For monotonic loading, the simulations were performed with a plasticity-based model, while for cyclic loading a combined damage-plasticity model was used. The combined model was necessary in order to correctly capture the decrease in the unloading stiffness and the permanent deformations after unloading. However, it was shown that the experimental observations could not be captured with the numerical model and consequently, the problem must be modified. Therefore, an imperfection or an additional bending component was added. It was shown that, with the modification, the experiments were simulated more accurately. This paper shows that comparing numerical simulations with experimental data should be done with great care. A fit of the simulations to the global data is not sufficient to conclude that the model can capture the real response. Local data in computations and from experiments should be compared. Consequently, the derivation of the material parameters from an experiment is not straightforward.

Acknowledgements

Financial support from the FWO-Vlaanderen (Fonds voorWetenschappelijk Onderzoek, Fund for Scientific Research - Flanders) for K. De Proft is gratefully acknowledged. G.N. Wells gratefully acknowledges the support of STW (Netherlands Technology Foundation). The authors also wish to thank the reviewer for valuable comments.

References

Moës, N., Dolbow, J. and Belytschko, T. (1999), "A finite element method for crack growth without remeshing", *Int. J. Num. Meth. Eng.*, **46**, 131–150.

Wells, G. N. and Sluys, L. J. (2001), "A new method for modeling cohesive cracks using finite elements", *Int. J. Num. Meth. Eng.*, **50**(12), 2667–2682.

Wells, G. N. (2001), "Discontinuous modelling of strain localization and failure", Ph. D. thesis, Delft University of Technology.

De Proft, K. (2003), "Combined experimental-computational study to discrete fracture of brittle materials", Ph. D. thesis, Vrije Universiteit Brussel.

Carol, I., Prat, P. C. and Lopez, C. M. (1997), "Normal/shear cracking model: application to discrete crack analysis", *J. Eng. Mech.*, **123**, 765–773.

Simo, J. C., Oliver, J. and Armero, F. (1993), "An analysis of strong discontinuities induced by strain-softening in rate-independent inelastic solids", *Comut. Mech.*, **12**, 277–296.

Oliver, J., Cervera, J. and Manzoli, O. (1999), "Strong discontinuities and continuum plasticity 20 models: the strong discontinuity approach", *Int. J. Plasticity.*, **15**, 319–351.
Oliver, J. (2000), "On the discrete constitutive models induced by strong discontinuity kinematics and continuum constitutive equations", *Int. J. Solids Struct.*, **37**, 7207–7229.
Simo, J. C. and Ju, J. W. (1987) "Strain-and stress-based continuum damage models - I. formulation, II. computational aspects", *Int. J. Solids Struct.*, **23**(7), 821–869.

CC